Orbital
The electronic journal of chemistry

the electronic journal of chemistry

Full Paper | http://dx.doi.org/10.17807/orbital.v17i5.22919

Eco-friendly Synthesis and Characterization of Bioactive Iron Oxide Nanoparticles Using *Tagetes erecta* Leaf Extract for Antioxidant and Anti-Corrosion Application

Shobhit Sharma, Ruchi Bharti*, Ajay Thakur, Renu Sharma , and Monika Verma

In this study, we present a sustainable and efficient approach for synthesizing bioactive iron oxide nanoparticles (FeO NPs) using *Tagetes erecta* leaf extract, an eco-friendly and readily available biological resource. The green synthesis method not only eliminates the need for hazardous chemicals but also leverages the plant's bioactive compounds, which act as natural reducing and stabilizing agents. The synthesized FeO NPs were meticulously characterized through various advanced techniques, including UV-visible spectroscopy, FTIR, SEM-EDX, XRD, and DLS, confirming their formation, structural attributes, and spherical morphology. The antioxidant potential of FeO NPs was evaluated using DPPH and ABTS assays, revealing significant free radical scavenging activities, particularly in the DPPH assay with a scavenging percentage of 92.91%, comparable to standard antioxidants like ascorbic and gallic acids. Furthermore, the FeO NPs demonstrated exceptional anti-corrosion capabilities, achieving a maximum inhibition efficiency of 79.5% at a concentration of 40 mg, as verified through electrochemical impedance spectroscopy and potentiodynamic polarization methods. This was supported by weight-loss studies, which highlighted superior performance at higher concentrations. By utilizing *Tagetes erecta* leaves, known for their rich bioactive profile and medicinal properties, this research advances the field of green nanotechnology. It underscores the feasibility of developing multifunctional nanoparticles for applications in environmental protection, biomedicine, and industrial corrosion prevention. This work provides a promising framework for integrating sustainability into nanomaterial synthesis while enhancing their functional properties.

Graphical abstract

Keywords

Antioxidant activities
Anti-Corrosion activities
Green Synthesis
Iron Nanoparticles
Metal oxides

Article history

Received 26 Feb 2025
Revised 08 Aug 2025
Accepted 11 Sep 2025
Available online 15 Dec 2025

Handling Editor: Ana C. Micheletti

1. Introduction

University Institute of Sciences, Department of Chemistry, Chandigarh University, Mohali, Punjab-140413, India. *Corresponding author: E-mail: **ruchi.uis@cumail.in**

The rapid advancement of nanotechnology has sparked significant breakthroughs in various scientific fields, catalyzing research into the synthesis and applications of nanoparticles [1-5]. Metallic nanoparticles, particularly iron oxide nanoparticles (FeO-NPs) [6], have gained substantial attention due to their unique physicochemical properties such as high surface area, excellent thermal stability, and strong magnetic behavior. These properties make them highly versatile, with applications in areas ranging from biomedical engineering to environmental remediation and industrial corrosion prevention [7-9]. However, conventional methods for synthesizing these nanoparticles often involve hazardous chemicals and require high energy input, leading to potential environmental and safety risks. In response to these challenges, green synthesis methods have emerged as eco-friendly and sustainable alternatives (Figure 1) [10-12]. These methods harness biological agents like plant extracts, fungi, and bacteria as natural reducing and stabilizing agents, minimizing the use of toxic reagents and reducing environmental impact. This approach aligns with the growing emphasis on sustainability and safety in scientific research and industrial practices [13].

Fig. 1. Key merits of the green synthesis.

In exploring the scope of green synthesis, our study introduces *Tagetes erecta* (commonly known as marigold) leaf extract as a novel agent for producing FeO NPs. The choice of *Tagetes erecta* is significant due to its rich bioactive molecules known for their antioxidant, antimicrobial, and anti-inflammatory properties [14-17]. Compared to other commonly used agents in nanoparticle synthesis, such as green tea or *Citrus sinensis*, which have been extensively studied [18, 19], *Tagetes erecta* presents a unique set of bioactive compounds that contribute to the synthesis process in potentially more effective ways (Figure 2). This research fills a notable gap in the literature where limited studies have focused on using this plant specifically for iron oxide nanoparticle synthesis, thereby adding a novel perspective to the field of green nanotechnology [20-22]. In this research, we successfully utilized *Tagetes erecta* leaf extract for the eco-friendly synthesis of iron oxide nanoparticles, highlighting our commitment [23-28] to sustainable production methods (Table 1). By leveraging natural resources, we not only reduced chemical waste but also enhanced the nanoparticles' functionality for potential use in health and environmental applications.

Our findings contribute to Sustainable Development Goal (SDG) 12, which emphasizes responsible consumption and production patterns, specifically targeting the reduction of chemical wastes and the promotion of sustainable industrial processes. Additionally, by showcasing the dual functionality of the synthesized nanoparticles—both as antioxidants and anti-corrosive agents—our research supports SDG 3, which focuses on good health and well-being, through the potential development of biomedical applications for these nanoparticles.

Fig. 2. *Tagetes erecta* Plant.

2. Material and Methods

2.1 Materials

Ferrous sulfate heptahydrate ($FeSO_4 \cdot 7H_2O$) was selected as the primary precursor for iron ions, sourced from Sigma Aldrich to ensure reagent-grade quality. Additional chemicals, including ABTS (2,2'-azino-bis(3-ethylbenzothiazoline-6-sulfonic acid)) and DPPH (2,2-diphenyl-1-picrylhydrazyl), were similarly acquired from Sigma Aldrich and used as-is without further purification to maintain the accuracy of the experiment. These reagents provided the basis for evaluating antioxidant and anticorrosive properties.

2.2 Preparation of Plant Extract

Fresh marigold (*Tagetes erecta*) leaves were collected from the herbal garden at Chandigarh University, known for their abundance of bioactive compounds. The leaves were initially washed with tap water to remove visible impurities and then rinsed four to five times with distilled water to ensure thorough cleaning. The cleaned leaves were finely chopped, and 50 grams of the prepared plant material was combined with 500 mL of distilled water. This mixture was heated to approximately 100°C using a heating mantle and maintained at that temperature for one hour to facilitate extraction. The resulting solution was filtered using Whatman filter paper to remove plant debris, yielding a clear extract. This extract was stored at 5–10°C until further use in nanoparticle synthesis.

2.3 Synthesis of Iron Oxide Nanoparticles (FeO NPs)

The synthesis involved dissolving $FeSO_4 \cdot 7H_2O$ in distilled water to create a 0.1M solution, which was then loaded into a 50 mL burette for precision. A 50 mL conical flask containing the marigold extract was placed on a magnetic stirrer, and the iron solution was added dropwise. The continuous stirring facilitated the uniform distribution of iron ions and bioactive compounds, initiating a color change that indicated nanoparticle formation. The mixture was stirred for three hours to ensure a complete reaction, after which it was

centrifuged to separate the synthesized nanoparticles from the supernatant. The precipitate was washed multiple times with ethanol and distilled water to remove impurities, and then dried at 30°C in an oven. The dried FeO NPs were collected and stored for subsequent analysis.

Table 1. *Tagetes erecta* Leaf Extract in Nanoparticle Synthesis: Literature Summary

S.No	Type of Nanoparticles	Study Highlights	Reference
1	Zinc Oxide Nanoparticles (ZnO NPs)	Green synthesis and characterization of ZnO NPs using Tagetes erecta leaf extract.	Chowdhury, A. S., Islam, M. M., & Ghosh, A. (2024). Proceedings of the 14th International Conference on Mechanical Engineering (ICME 2023) [29].
2	Silver Nanoparticles (AgNPs)	Structural, optical, chemical, and morphological studies of AgNPs synthesized using Tagetes erecta.	Katta, V. K. M., & Dubey, R. S. (2021). Materials Today: Proceedings, 45, 794-798 [30].
3	Silver Nanoparticles (AgNPs)	Antioxidant activity of AgNPs synthesized from Tagetes erecta leaves.	Erenler, R., et al. (2021). International Journal of Chemistry and Technology, 5(2), 141-146[31].
4	Silver Nanoparticles (AgNPs)	Eco-friendly phytosynthesis of AgNPs using Tagetes erecta leaf extract.	Dhuldhaj, U. P., et al. (2012). Nusantara Bioscience, 4(3) [32].
5	Silver Nanoparticles (AgNPs)	Synthesis of AgNPs via ascorbic acid and polyphenols in Tagetes erecta extract; antioxidant property studied.	Tyagi, P. K., et al. (2021). Journal of Nanomaterials, 2021(1), 6515419 [33].

2.4 Characterization of Nanoparticles

Comprehensive characterization of FeO NPs was conducted using multiple advanced techniques:

FT-IR Spectroscopy: FTIR analysis was performed using a PerkinElmer FT-IR spectrometer equipped with a KBr beam splitter and a DTGS detector (deuterated triglyceride sulfate). The spectra were recorded in the range of 4000–400 cm^{-1} with a resolution of 4 cm^{-1}, using KBr pellets prepared with dried FeO NPs. The technique identified functional groups involved in the reduction and stabilization of nanoparticles by *Tagetes erecta* extract [34].

SEM-EDX Analysis: The morphological features and elemental composition of FeO NPs were analyzed using a HITACHI SU8010 SEM equipped with an EDX detector coated with platinum (Pt) for enhanced imaging resolution. SEM micrographs were captured at magnifications ranging from 5000x to 50,000x, while EDX confirmed the presence of iron and oxygen, validating the purity and composition of the synthesized nanoparticles [35].

XRD Analysis: The crystalline structure and phase composition of FeO NPs were analyzed using an X'PERT PRO X-ray diffractometer equipped with a Cu-Kα radiation source (λ = 1.5406 Å). The XRD patterns were recorded in the 2θ range of 10° to 80°, with a step size of 0.02° and a scan speed of 0.5° per second. The observed broad diffraction peaks indicated the amorphous or poorly crystalline nature of FeO NPs, which is typical of nanoparticles synthesized via green methods using plant extracts [36].

DLS Analysis: The particle size distribution and colloidal stability of FeO NPs were evaluated using a Litesizer DLS (Anton Paar). The measurements were performed at 25°C in distilled water with a scattering angle of 173°. The Z-average particle size and polydispersity index (PDI) were calculated to assess the size uniformity of nanoparticles [37].

2.5 Antioxidant Activity Assays

2.5.1 DPPH Assay

The DPPH assay evaluated the free radical scavenging capability of the FeO NPs. A solution of the nanoparticles (1 mg/mL) was mixed with 3 mL of a DPPH solution (4 mg in methanol). After incubation in the dark for 30 minutes at room temperature, the absorbance at 517 nm was measured using the Shimadzu UV-2450 spectrophotometer [38]. The percentage of radical scavenging was calculated using:

- $\boldsymbol{DPPH\ Scavenging\ (\%) = [(A_{(control)} - A_{(sample)} / A_{(control)}] \times 100}$

where $A_{control}$ represents the absorbance of the control sample (DPPH solution without FeO NPs), and A_{sample} represents the absorbance of the sample containing FeO NPs.

2.5.2 ABTS Assay

The ABTS assay involved generating ABTS radicals through an oxidizing reaction. The antioxidant capacity was assessed by mixing FeO NPs with the radical solution and measuring the decrease in absorbance at 734 nm [39]. The percentage inhibition was calculated using:

- $\boldsymbol{ABTS\ Inhibition\ (\%) = [(A_{(control)} - A_{(sample)} / A_{(control)}] \times 100}$

where $A_{control}$ represents the absorbance of the control sample (ABTS solution without FeO NPs), and A_{sample} represents the absorbance of the sample containing FeO NPs.

2.6 Anticorrosion Activity

The anti-corrosive properties were studied using electrochemical methods like Electrochemical Impedance Spectroscopy (EIS) and Weight Loss Method. Electrochemical Impedance Spectroscopy (EIS) is a setup with a steel working electrode (1 cm^2), calomel reference electrode, and platinum counter electrode was used. Nyquist and Bode plots were analyzed to assess the impedance and corrosion inhibition. Potentiodynamic Polarization (PDP): [40]. Tafel curves were plotted by scanning the potential between -0.1 V and 0.1 V. Parameters such as corrosion potential (E_corr) and corrosion current density (I_corr) were recorded to determine the inhibitor efficiency. The best performance was observed at a 40 mg concentration, showing a maximum inhibition efficiency of 79.5%. Whereas in weight loss method [36], steel samples were weighed before and after immersion in

solutions with varying concentrations of FeO NPs (10, 20, 30, 40 mg). The weight loss was measured over 24 and 48 hours, calculating corrosion rate, surface coverage, and inhibition efficiency. Each experiment was repeated three times for accuracy, confirming the reproducibility and reliability of results.

3. Results and Discussion

The utilization of *Tagetes erecta* leaf extract proved to be an effective method for synthesizing iron nanoparticles in a straightforward and environmentally conscious manner. Marigold leaves were chosen for their abundance of bioactive compounds and functional groups, making them well-suited for nanoparticle synthesis. These leaves possess reductant properties, allowing biomolecules within them to efficiently reduce iron ions, facilitating the formation of iron oxide nanoparticles from iron salts. As the ferrous sulfate heptahydrate solution was added, a noticeable change in color occurred, indicating the initiation of the reaction between the iron ions and the compounds present in the marigold leaf extract.

3.1 FT-IR Analysis

FT-IR spectra of the Tagetes erecta extract (Figure 3) indicated distinct peaks for functional groups engaged in nanoparticle synthesis. The broadband absorption at 3310 cm¹ is mainly due to O–H stretching vibrations, which can be attributed to hydroxyl groups in bioactive phytochemicals (e.g., flavonoids and phenolics) and the presence of water molecules inherent in the plant extract. These hydroxyl-bearing molecules play a key role in metal ion reduction and nanoparticle stabilization. Although the role of water cannot be eliminated, the role of plant-derived hydroxyl is amply supported by the established phytochemical composition of Tagetes erecta. This was followed by peaks at 1633 cm^{-1} (carbonyl groups) and 2117 cm^{-1} (indicative of alkenes/alkynes). Post-synthesis (Figure 4), the FeO NPs displayed distinct peaks at 3197 cm^{-1} (OH group vibrations), shifts indicating interactions between the bioactive compounds and iron ions, and new peaks like 1581 cm^{-1} (aromatic ring vibrations). These changes validate the involvement of the extract's compounds in reducing and stabilizing. Conclusion: The formation of FeO NPs confirmed by the peak between 575 cm^{-1} and 474 cm^{-1}, which is absent in the FTIR spectrum of plant extract [41]. The FT-IR analysis ensures the successful synthesis, with functional groups in the extract participating in the capping and formation of FeO NPs.

3.2 SEM-EDX Analysis

The morphology and elemental composition of the synthesized FeO nanoparticles (FeO NPs) were examined using a HITACHI SU8010 scanning electron microscope equipped with an energy dispersive X-ray (EDX) detector. The analysis revealed crucial insights into the structural and compositional attributes of the nanoparticles. The SEM images (Figure 5A) highlighted the irregular, angular morphology with distinct sharp edges and the surface characteristics of the FeO NPs, indicating successful reduction of iron ions [42] and stabilization by bioactive compounds in *Tagetes erecta* extract. The absence of significant aggregation suggests effective dispersion during synthesis.

In (Figure 5B). At higher magnifications, the consistency in particle size becomes more evident, showcasing a narrow size distribution. This uniformity is crucial for applications requiring reproducible nanoparticle performance, such as biomedicine and anti-corrosion.

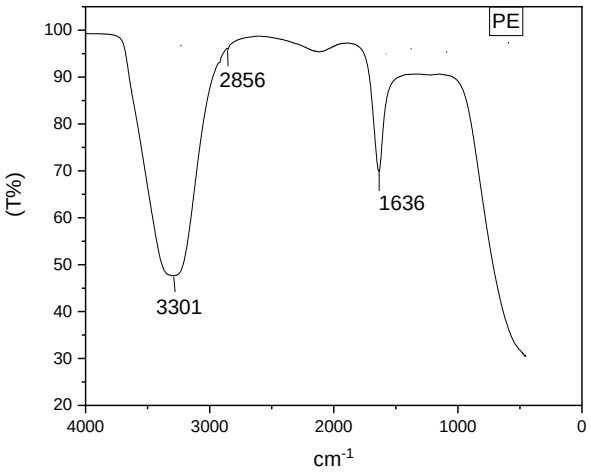

Fig. 3. FTIR of *Tagetes erecta* leaf extract.

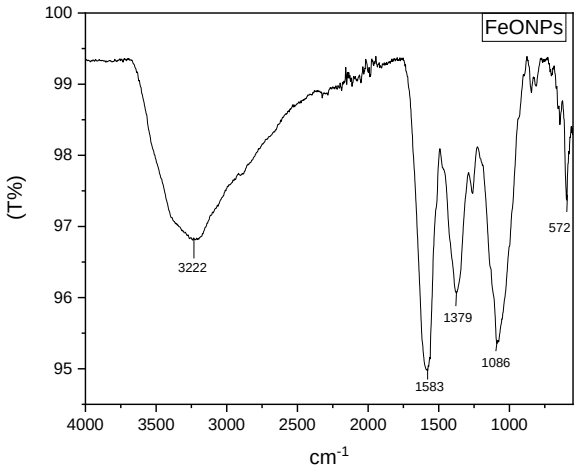

Fig. 4. FTIR of iron oxide nanoparticles (FeO NPs).

Whereas, the EDX spectrum complemented (Figure 6) the SEM analysis by confirming the elemental composition of the synthesized FeO NPs: The primary elements detected were iron (46.36% by mass) and oxygen (53.64% by mass), validating the formation of iron oxide nanoparticles with minimal impurities (Table 2). The Fe:O ratio corresponds to typical forms of iron oxides, such as Fe_2O_3 or Fe_3O_4, further confirming the identity of the nanoparticles. Notably, no significant peaks corresponding to contaminants were observed, indicating the high purity of the synthesized FeO NPs. The combined SEM and EDX analyses painted a comprehensive picture of the synthesized nanoparticles. The uniform spherical morphology and high elemental purity underscore the effectiveness of using *Tagetes erecta* leaf extract in the green synthesis of FeO NPs. The stability imparted by the bioactive compounds ensures minimal aggregation, making these nanoparticles highly suitable for their intended application.

3.3 DLS analysis.

The DLS data (Figure 7) provided insights into particle size distribution and uniformity. The Z-average size of 385.8 nm

and a low polydispersity index (PI) of 0.2714 indicated a relatively homogeneous population of Nanoparticles [43]. The intercept value of 0.9605 and minimal fit error (0.001843) emphasized reliable size measurements, with 92.86% of particles within the targeted size range. The peak mean by intensity (413.5 nm) confirmed the most abundant particle size. Here, the DLS analysis demonstrated the formation of FeO NPs with a controlled size distribution, suggesting high synthesis quality

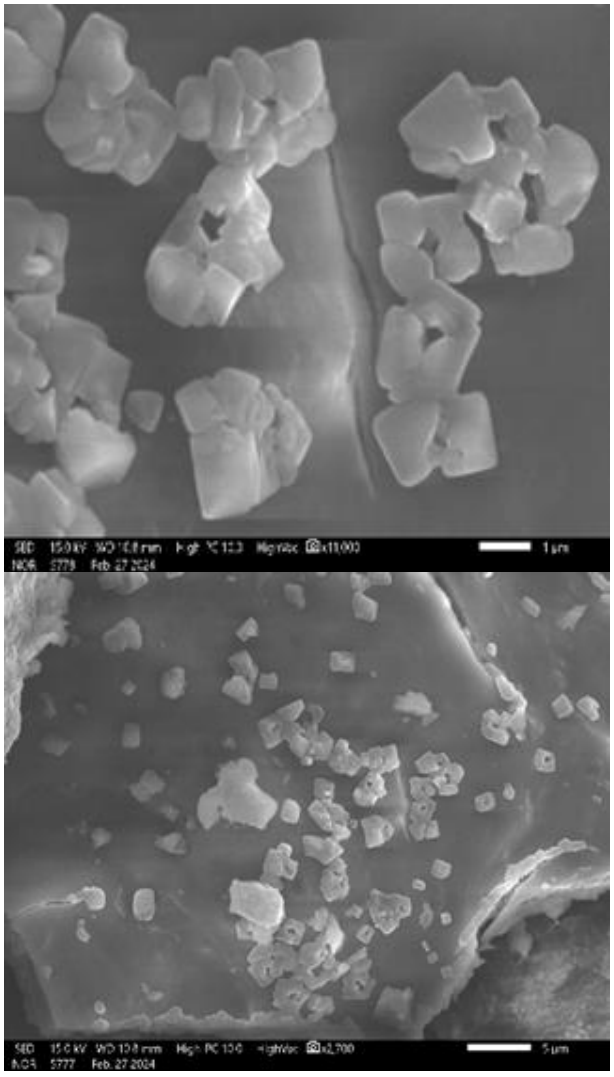

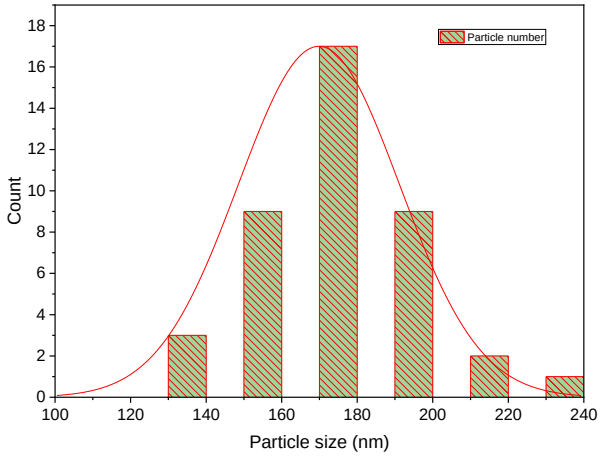

Fig. 5. Particle size distribution histogram from SEM images.

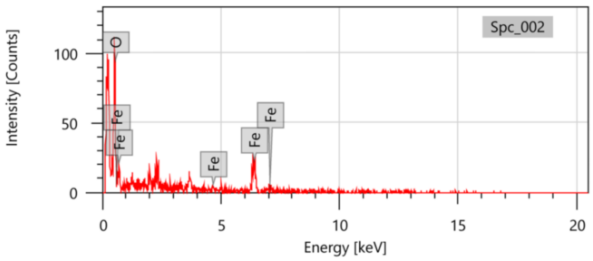

Fig. 6. SEM EDX of synthesized FeO-NPs.

Table 2. Elemental composition of Synthesised NPs.

Element	Line	Mass%	Atom%
O	K	53.64 ± 2.01	80.15 ± 3.00
Fe	K	46.36 ± 2.74	19.85 ± 1.17
Total		100.00	100.00

3.4 XRD Analysis.

XRD analysis (Figure 8) revealed broad peaks at 2θ values such as 26.6°, 31.6°, and 40.6°, indicating the successful synthesis of iron oxide nanoparticles. Peaks around 26°-28° and 31°-32° are associated with FeO phases [44]. The sharpness and intensity of the peaks suggest that the nanoparticles exhibit a crystalline structure. By using the Scherrer formula, the average size of crystalline domains within a material based on the width of peaks observed in its X-ray diffraction pattern is calculated. The formula is expressed as:

$D = k\lambda / \beta\cos(\theta)$

Where:

D is the average crystal size,

k is the Scherrer constant (usually around 0.9, depending on the shape of the crystallites),

λ is the wavelength of the X-ray radiation,

β is the FWHM of the XRD peak,

θ is the Bragg angle

The average crystal size of the synthesised NPs was determined to be 20nm, and iron oxide nanoparticles typically exhibit crystalline size ranging from 16nm to 56nm based on the synthetic method. Overall, the XRD analysis highlights the formation of well-crystallized FeO nanoparticles with potential structural consistency.

The combined analyses—FT-IR, SEM-EDX, DLS, and XRD—demonstrated that the eco-friendly synthesis of FeO NPs using *Tagetes erecta* was successful. The FT-IR spectra confirmed functional group interactions, SEM-EDX validated morphology and composition, DLS showed consistent size distribution, and XRD suggested an amorphous structure. The desired nanoparticles were indeed formed, offering potential for applications in biomedical and environmental fields. Improvements could focus on refining characterization techniques and synthesis conditions to optimize particle properties.

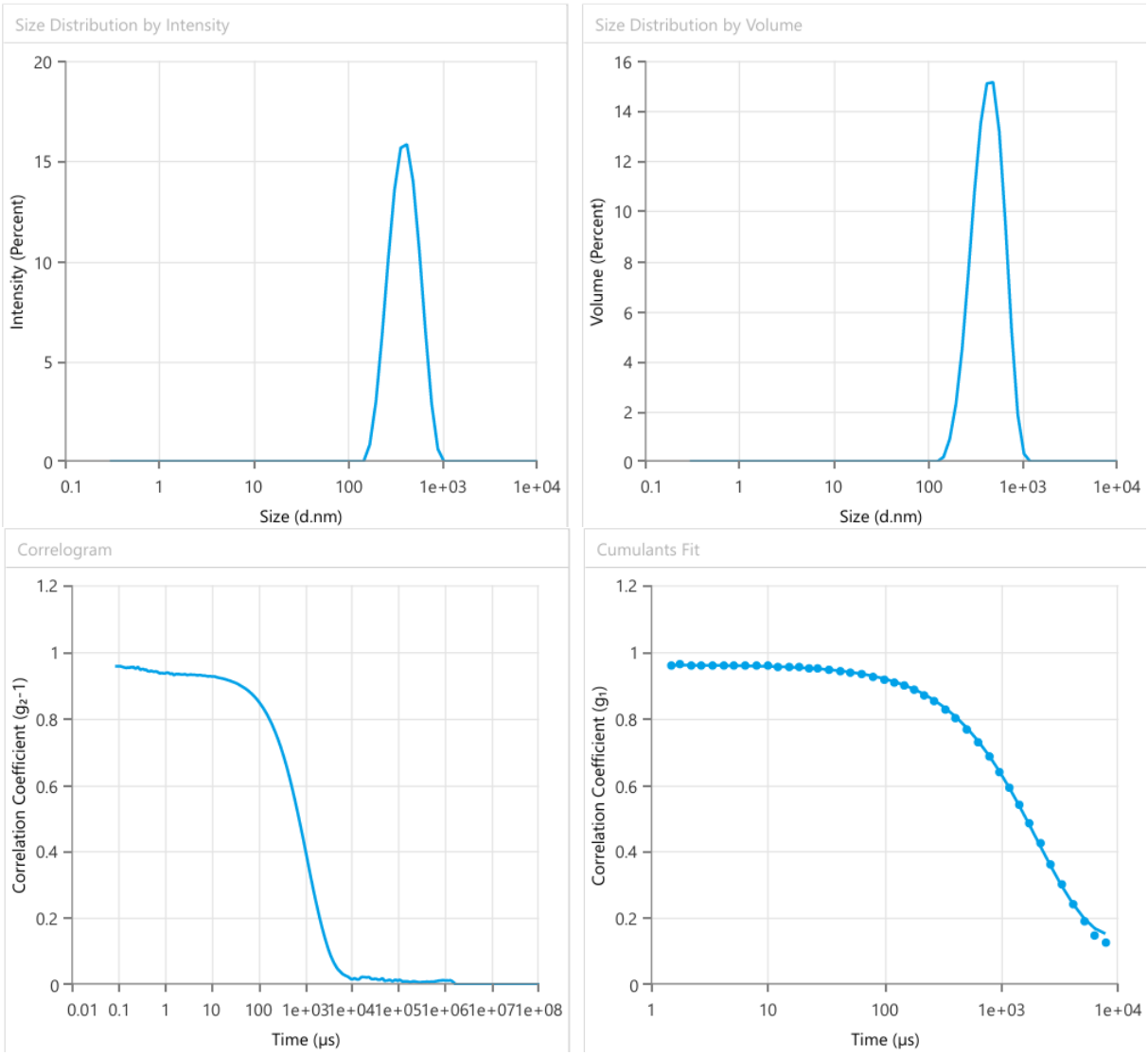

Fig. 7. Size distribution (a, b), Correlogram (c), and Comulants fit diagram (d).

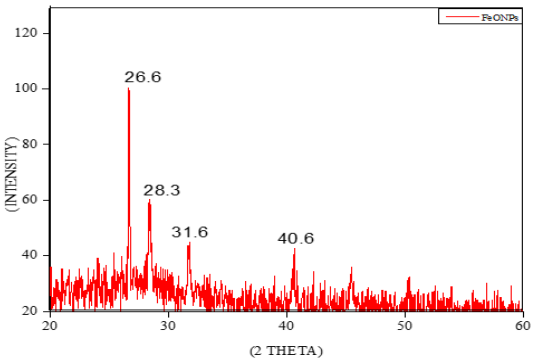

Fig. 8. XRD patterns of Synthesised FeO NPs.

3.5 Antioxidant Activity

Following the successful synthesis and characterization of FeO NPs, their antioxidant potential was assessed using DPPH and ABTS assays. These assays are well-established for evaluating free radical scavenging capabilities, which are critical for applications in biomedicine and environmental protection.

3.5.1 DPPH Assay

The DPPH assay measures the ability of nanoparticles to neutralize free radicals through electron donation. The FeO NPs demonstrated a high radical scavenging activity with a percentage of 92.91±0.002% (Table 3). This value indicates a strong antioxidant effect, comparable to that of the standard compound, gallic acid (91.76±0.62%), and slightly higher than ascorbic acid (89.52±0.89%) [45]. The high antioxidant activity suggests that the bioactive compounds from the *Tagetes erecta* leaf extract, which remained as capping agents on the nanoparticle surface, contributed to the enhanced free radical scavenging capability. The DPPH results are accurate and indicate that FeO NPs exhibit significant antioxidant potential. The small error margin (±0.002%) improves the reliability of these results, confirming that the synthesized nanoparticles can effectively participate in antioxidant mechanisms.

3.5.2 ABTS Assay

The ABTS assay complements the DPPH test by measuring the ability of antioxidants to quench ABTS radicals. In this study, the FeO NPs showed a lower scavenging activity of 11.63±0.002% compared to gallic acid (96.65±0.15%) and ascorbic acid (97.53±0.15%). This discrepancy between the DPPH and ABTS assays may be due to the differences in the

mechanisms by which these assays function; DPPH primarily measures hydrophobic antioxidant activity, while ABTS can capture both hydrophilic and lipophilic properties [50]. The significant difference in ABTS activity suggests that the synthesized FeO NPs might exhibit stronger activity in environments more closely mimicked by the DPPH assay conditions. While the FeO NPs showed excellent performance in the DPPH assay, their lower activity in the ABTS test indicates that their antioxidant efficacy might be more selective and context-dependent.

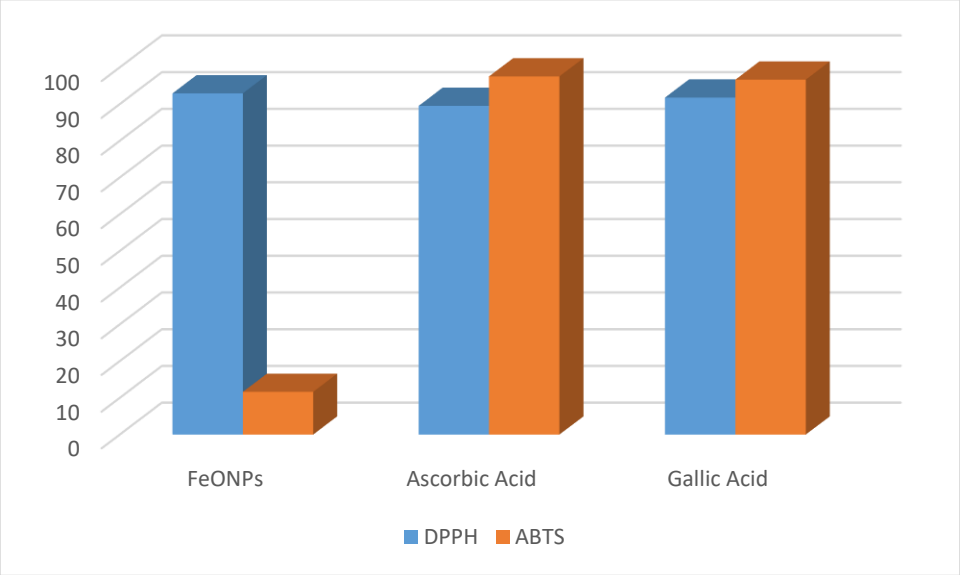

Fig. 9. Comparison of antioxidant activities.

Table 3. Antioxidant activities against DPPH and ABTS assays.

Sample	DPPH	ABTS	REFERENCES
FeONPs	92.91 ± 0.002	11.63 ± 0.002	Present work
Ascorbic Acid	89.52 ± 0.89	97.53 ± 0.15	[46]
Gallic Acid	91.76 ± 0.62	96.65 ± 0.15	[46]
FeONPs by V.faba	90 ±0.01	91 ± 0.02	[47]
FeONPs by *Bacillus circulans*	39.44%	35.44%	[48]
FeONPs by Inedible borassurflabellifer	85.53%	-	[49]

The FeO nanoparticles prepared from *Tagetes Eeecta* leaf extract have significant antioxidant activity, especially in the DPPH assay, indicating their potential as efficient natural antioxidants. Their impressive DPPH scavenging capacity can be attributed to the presence of bioactive phytochemicals in the *Tagetes erecta* extract, which function as both capping and stabilizing agents. These molecules, for example, flavonoids, phenols, and terpenoids, stay bound to the nanoparticle surface, increasing their electron donation ability and facilitating effective neutralization of DPPH free radicals. The small size and high surface area of the developed FeONPs also offer more active sites, further enhancing their antioxidant activity. The synergistic effect of green synthesis and phytochemical functionalization is the reason why such FeO NPs exhibit improved antioxidant activity as opposed to conventional chemically synthesized nanoparticles. The lower ABTS assay performance highlights a selective behavior that warrants further investigation. The table data are consistent and correctly presented, supporting the interpretation. This aligns with prior research highlighting the biocompatibility and bioactive antioxidant properties of iron oxide nanoparticles.

3.6 Anticorrosive Activity

In continuation of the evaluation of antioxidant properties, the anticorrosive potential of FeO NPs synthesized using *Tagetes erecta* leaf extract was rigorously analyzed using electrochemical techniques, including Nyquist plots, Bode plots (A and B), and Tafel plots [51]. Additionally, a weight loss method provided further insight into the corrosion inhibition performance of FeO NPs compared to the plant extract.

3.6.1 Nyquist Plot Analyses

Nyquist plots (Figures 10a and 10b) provide information about the metal-electrolyte interface. The semicircular nature of these plots indicates the effectiveness of the anticorrosive agent. FeO NPs: The Nyquist plot for FeO NPs showed an increased diameter of the semicircle with higher concentrations, peaking at 40 mg, indicating significant resistance to charge transfer. This increase suggests enhanced protective behavior, correlating with the effectiveness of the synthesized nanoparticles in inhibiting corrosion. Plant Extract: Comparatively, the plant extract also exhibited a semicircular pattern, but with smaller diameters across all concentrations, implying less effective corrosion inhibition.

The FeO NPs demonstrated superior performance in forming a barrier that hindered the electrochemical reaction between the steel surface and the corrosive medium.

3.6.2 Bode Plot Analysis (A and B)

Bode plots help visualize impedance data more comprehensively through phase angle and modulus plots.

Bode A Plot for FeO NPs, as shown in Figure 11a, the impedance magnitude at 40 mg concentration was significantly higher than at lower concentrations, reflecting increased stability and reduced corrosion. The phase angle was also at its peak at this concentration, indicating strong capacitive behavior due to the formation of a protective layer [52].

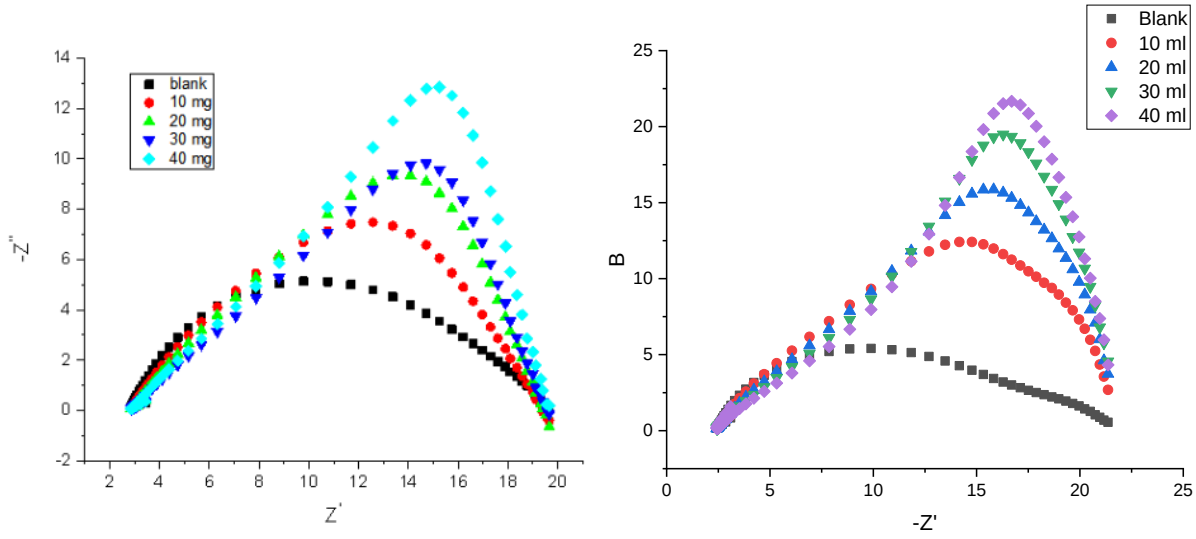

(a) (b)

Fig. 10. (a) Nyquist Plot for NPs for Different Concentrations. b) Nyquist Plot for Plant Extract at Different Concentrations.

Bode A Plot for Plant Extract as shown in Figure 11b, revealed that the plant extract's impedance was lower across all concentrations, with moderate phase angles, pointing to a less robust protective layer.

However, Bode B Plot for FeO NPs and Plant Extract mentioned in figures 12a and 12b displayed a clearer comparison. The 40 mg concentration of FeO NPs consistently exhibited a higher phase angle and impedance, confirming better corrosion resistance compared to the plant extract. The Bode plot analysis reinforced that FeO NPs provided better corrosion inhibition by enhancing the protective layer's electrochemical properties.

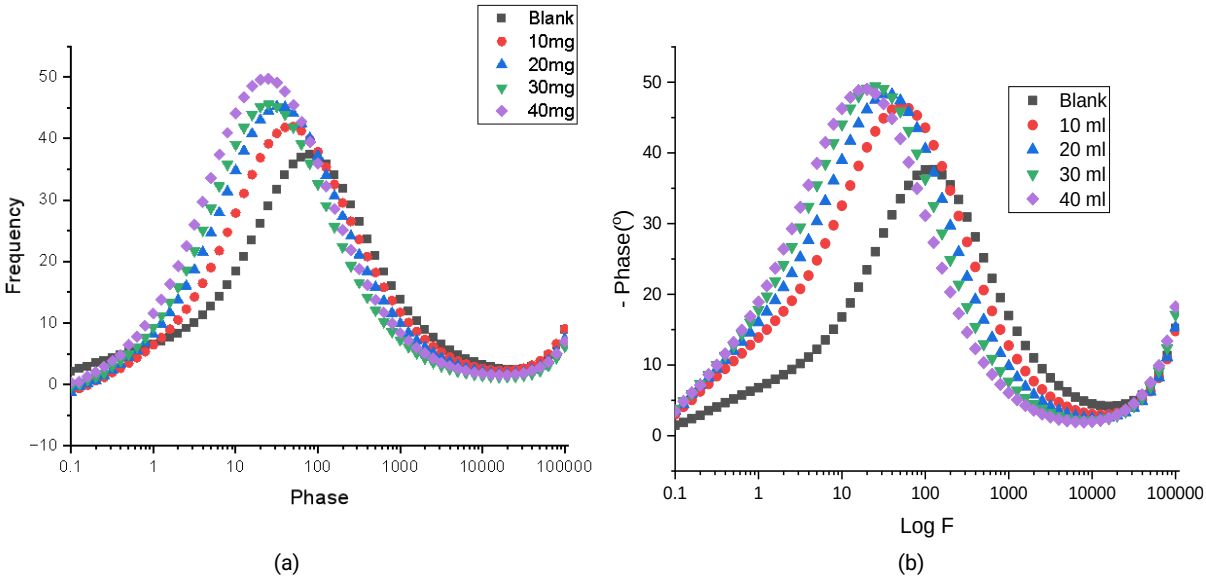

(a) (b)

Fig.11. (a) Bode A Plot for NPs at different concentrations. (b) Bode A Plot for plant extract at different concentrations.

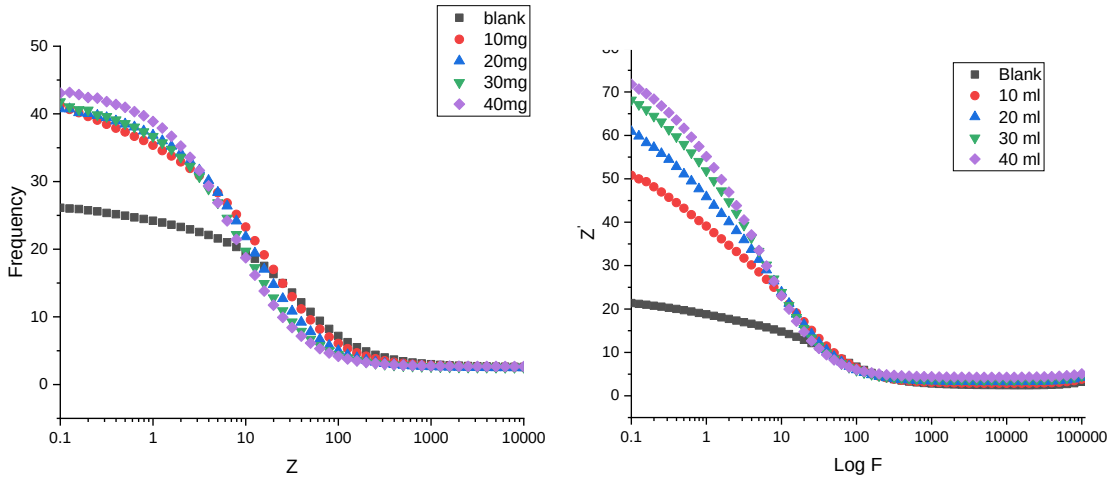

(a) (b)

Fig. 12. (a) Bode B Plot for NPs at different concentrations. (b) Bode B Plot for Plant extract at different concentrations.

3.6.3 Tafel Plot Analysis

Tafel plots given in Figures 13a and 13b, illustrated the polarization behavior by showing the relationship between potential and current density, helping to derive the corrosion current (I_{corr}) and corrosion potential (E_{corr}).

The Tafel plot for FeO NPs showed a shift in the corrosion potential (E_corr) and a significant reduction in corrosion current (I_{corr}) at 40 mg, leading to an efficiency of 79.5% (Table 4). This indicates strong anodic and cathodic inhibition, implying a mixed-type inhibitor [53]. The plant extract exhibited less pronounced shifts in (E_{corr}) and a higher (I_{corr}) across concentrations, resulting in lower overall efficiency (Table 5). The data from the Tafel plots confirmed that FeO NPs were more effective as corrosion inhibitors due to their ability to lower the corrosion rate by forming a stronger protective film on the metal surface.

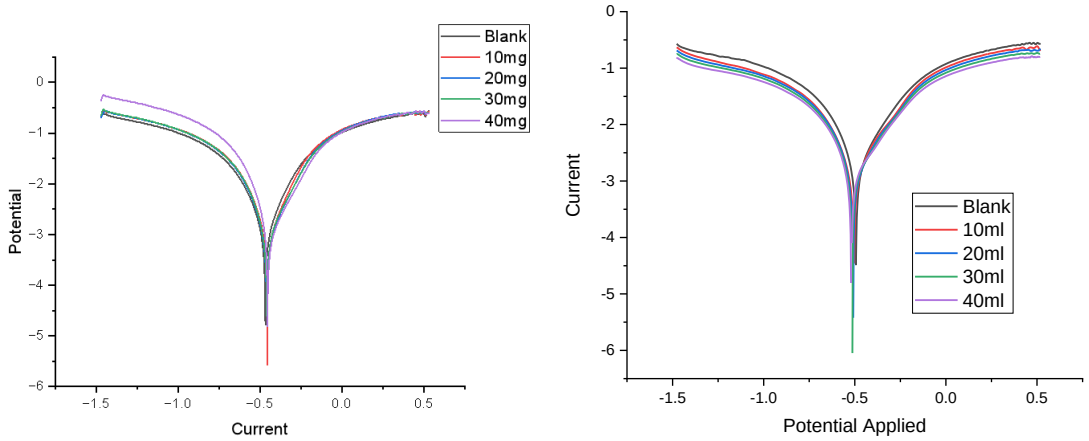

(a) (b)

Fig. 13. (a) Tafel Plot for NPs at different concentrations. (b) Tafel Plot for Plant extract at different concentrations.

Table 4. Tafel Calculation for Plant Extract (Polarization Parameters).

CONC. (mg/ml)	Ecorr (V vs. SCE)	Icorr(A/cm^{-3}	βa(V/decade)	βa(V/decade)	EFFICIENCY
0	-0.216	1.0×10^{-4}	1.316	0.416	-
10	-0.338	1.1×10^{-4}	1.209	0.726	71.9%
20	-0.342	2.5×10^{-4}	0.568	1.310	65.3%
30	-0.422	1.3×10^{-3}	0.345	0.883	67.2%
40	-0.231	2.4×10^{-4}	1.847	1.820	78.5%

Table 5. Tafel Calculation For Nps (Polarization Parameters)

CONC. (mg/ml)	Ecorr (V vs. SCE)	Icorr(A/cm^{-3}	βa(V/decade)	βa(V/decade)	EFFICIENCY
0	-0.215	1.0×10^{-4}	1.300	0.400	-
10	-0.328	2.8×10^{-5}	1.180	0.700	72.4%
20	-0.340	3.4×10^{-5}	0.600	1.200	66.2%
30	-0.410	3.0×10^{-5}	0.400	0.850	69.8%
40	-0.230	2.1×10^{-5}	1.800	1.750	79.6%

3.6.4 Weight Loss Method

The weight loss method is a straightforward, reliable, and widely used technique to evaluate the corrosion rate of metals in the presence of inhibitors such as plant extracts and nanoparticles (NPs). It measures the mass difference of a metal sample before and after exposure to a corrosive medium. This approach provides direct evidence of material degradation, which helps in determining the corrosion rate, surface coverage, and inhibition efficiency of the tested anticorrosive agents.

Fig. 11. Weight loss method for blank, 10 mg, 20 mg, 30 mg, 40 mg of FeO-NPs.

Tables 6 and 7 show the Weight Loss (g) for FeO-NPs, which indicates the amount of material lost due to corrosion. A decrease in weight loss with increased concentration of FeO NPs (e.g., 40 mg showing 0.289 g loss) suggests enhanced corrosion resistance. The fraction of the metal surface protected by the anticorrosive agent. Higher values (e.g., 0.465 for 40 mg concentration) indicate better surface protection. Inhibition Efficiency (%) represents the percentage reduction in corrosion rate due to the inhibitor. The efficiency peaks at 60% for the highest concentration, signifying the superior performance of FeO NPs at higher doses. Here, corrosion rate was measured in terms of mass loss per unit area and time, while lower rates implied better anticorrosive performance [54].

Efficiency Calculation Formula

Efficiency (%) = $((C_o - C_i) / C_o) \times 100$

Where:

- CR0C {R0}CR0 = Initial concentration
- CriC {Ri}CRi = Final (or residual) concentration

Table 6. Weight Loss Method of NPs for 24 h.

CONC. (mg)	WEIGHT LOSS (g)	SURFACE COVERAGE	EFFICIENCY (%)	CORROSION RATE
0	0.706	-	-	15.7085
10	0.370	0.475	47%	8.2325
20	0.314	0.555	55%	6.9865
30	0.307	0.565	56%	6.83075
40	0.289	0.590	60%	6.43025

Table 7. Weight Loss Method of NPs for 48 h.

CONC. (mg)	WEIGHT LOSS (g)	SURFACE COVERAGE	EFFICIENCY (%)	CORROSION RATE
0	1.321	-	-	14.696
10	0.657	0.502	50%	7.309
20	0.567	0.570	57%	6.307
30	0.546	0.586	58%	6.074
40	0.465	0.647	64%	5.173

Fig. 14. Weight Loss for blank, 10 mL, 20 mL, 30 mL and 40 mL.

Table 7 Highlights that the plant extract alone offered a moderate level of corrosion inhibition. For instance, a 40 mg concentration achieved 64% efficiency. However, the weight loss (0.314 g) was higher compared to FeO NPs at similar concentrations, which implies that the extract alone was less effective.

Surface coverage is also lower than that observed with FeO NPs, supporting this conclusion. However, in Table 9, the data showed a decline in inhibition efficiency over time (56% for 40 mg concentration after 48 hours), indicating that the plant extract's protective capability decreases with prolonged exposure.

Table 8. Weight Loss Method of Plant Extract for 24 h.

CONC. (mg)	WEIGHT LOSS (g)	SURFACE COVERAGE	EFFICIENCY (%)	CORROSION RATE
0	0.601	-	-	13.37225
10	0.327	0.451	45%	7.27575
20	0.318	0.470	47%	7.0755
30	0.300	0.500	50%	6.675
40	0.295	0.51	51%	6.656

Table 9. Weight Loss Method of Plant Extract for 48 h.

CONC. (mg)	WEIGHT LOSS (g)	SURFACE COVERAGE	EFFICIENCY (%)	CORROSION RATE
0	1.202	-	-	13.37225
10	0.601	0.499	50%	6.69725
20	0.580	0.517	51%	6.4525
30	0.544	0.546	54%	6.063125
40	0.521	0.566	56%	5.796125

Although by comparing both the tables of Weight loss method for Plant extract and Feo-NPs, it was observed that the data given in Tables 8 and 9 for FeO NPs revealed consistent performance over both 24 and 48 hours, suggesting that the synthesized nanoparticles maintained their protective properties. In contrast, the plant extract's efficacy diminishes over time. In conclusion, the higher concentrations of both the NPs and the extract lead to improved inhibition, but FeO NPs achieve greater efficiency even at comparable doses. Hence, FeO NPs outperformed the plant extract in all metrics—weight loss, surface coverage, and inhibition efficiency—highlighted the superior anticorrosive properties of the synthesized nanoparticles.

Therefore, While the pure *Tagetes erecta* extract exhibits good corrosion inhibition in the short term, FeO nanoparticles provide certain benefits related to long-term stability, hardness, and performance under extreme industrial conditions. The FeO NPs establish a uniform protective shield and retain their activity over time, whereas the plant extract can degrade or lose activity. Thus, it is necessary to use the FeO NPs for creating a more stable, reusable, and industrially applicable corrosion inhibitor.

4. Conclusions

In this work, we explored an eco-friendly way to synthesize iron oxide nanoparticles (FeO NPs) using *Tagetes erecta* leaf extract, tapping into the plant's natural bioactive compounds as reducing and stabilizing agents. This green synthesis method not only avoids harmful chemicals but also aligns with sustainable practices. We confirmed the successful formation of FeO NPs through a range of analytical techniques: UV-Vis spectroscopy showed their absorbance properties, FT-IR highlighted the functional groups and interactions, SEM-EDX revealed a spherical shape and elemental composition, DLS indicated uniform particle size, and XRD pointed to their amorphous or low-crystallinity nature. The antioxidant properties of these FeO NPs were impressive, especially in the DPPH assay, where they showed strong free radical scavenging comparable to standard antioxidants. This suggests they could be useful as natural antioxidants in biomedical applications. When we tested their anticorrosive properties, the results were equally promising. Using electrochemical techniques and the weight loss method, we found that FeO NPs outperformed the plant extract by a significant margin. They consistently showed high corrosion inhibition over 24 and 48 hours, with better surface coverage and inhibition efficiency, proving their ability to form a strong, protective layer on metal surfaces. Overall, this study highlights that FeO NPs synthesized using *Tagetes erecta* not only bring environmental benefits through green production but also have great potential for real-world applications. Their dual role as powerful antioxidants and effective anticorrosive agents makes them promising candidates for use in fields ranging from biomedicine to industrial corrosion prevention.

Acknowledgments

The authors are thankful to the Department of Chemistry, Chandigarh University, for providing the basic lab facilities and various characterization techniques for doing this work. Authors are also thankful to SAIF, Panjab University, and Amity University for providing the Analytical facilities for conducting this research.

Author Contributions

S.S. contributed to the experimental design, data collection, and analysis of the synthesized nanoparticles and wrote the manuscript. R.B. supervised the research work, conceptualized the study, and provided expertise in the green synthesis approach and revised and edited the manuscript, particularly in evaluating the applications of the nanoparticles. A.T. contributed significantly to the manuscript structure and technical content. R.S. and M.V. assisted in the characterization of the nanoparticles and in reviewing the work.

References and Notes

[1] Stark, W. J.; Stoessel, P. R.; Wohlleben, W.; Hafner, A. J. C. S. R. *Chem. Soc. Rev*. **2015**, *44*, 5793. [Crossref]

[2] Malik, S.; Muhammad, K.; Waheed, Y. *Molecules* **2023**, *28,* 661. [Crossef]

[3] Ndolomingo, M. J.; Bingwa, N.; Meijboom, R. *J. Mater. Sci.* **2020**, *55*, 6195. [Crossref]

[4] Ahmed, S. F.; Mofijur, M.; Rafa, N.; Chowdhury, A. T.; Chowdhury, S.; Nahrin, M.; Islam, A.; Ong, H. C. *Environ. Res.* **2022**, *204*, 111967. [Crossref]

[5] Bayda, S.; Adeel, M.; Tuccinardi, T.; Cordani, M.; Rizzolio, F. *Molecules* **2019**, *25*, 112. [Crossref]

[6] Kumar, P.; Thakur, N.; Kumar, K.; Kumar, S.; Dutt, A.; Thakur, V. K.; Gutierrez-Rodelo, C.; Thakur, P.; Navarrete, A.; Thakur, N. *Coord. Chem. Rev*.0 **2024**, *507*, 215750. [Crossref]

[7] Ates, B.; Koytepe, S.; Ulu, A.; Gurses, C.; Thakur, V. K. *Chem. Rev.* **2024**, *120*, 9304. [Crossref]

[8] Singh, J.; Singh, S.; Gill, R. *J. Electrochem. Sci. Eng.* **2023**, *13*, 63. [Crossref]

[9] Eliaz, N. *Materials* **2019**, *12*, 407. [Crossref]

[10] Saratale, R. G.; Saratale, G. D.; Shin, H. S.; Jacob, J. M.; Pugazhendhi, A.; Bhaisare, M.; Kumar, G. *ESPR* **2018**, *25*, 10164. [Crossref]

[11] Madani, M.; Hosny, S.; Alshangiti, D. M.; Nady, N.; Alkhursani, S. A.; Alkhaldi, H.; Al-Gahtany, S. A.; Ghobashy, M. M.; Gaber, G. A. *Rev.* **2022**, *11*, 731. [Crossref]

[12] Kumar, J. A.; Krithiga, T.; Manigandan, S.; Sathish, S.; Renita, A. A.; Prakash, P.; Prasad, B. N.; Crispin, S. *J. Clean. Prod*. **2021,** *324*, 129. [Crossref]

[13] Pansambal, S.; Oza, R.; Borgave, S.; Chauhan, A.; Bardapurkar, P.; Vyas, S.; Ghotekar, S. *Appl.Nanosci.* **2023**, *13*, 6067. [Crossref]

[14] Song, J. Y.; Jang, H. K.; Kim, B. S. *Process Biochem.* **2009**, *44*, 1133. [Crossref]

[15] Sachin, T. M.; Homraj, S. *Pharma Innov. J*. **2021**, *10*, 422. [Crossref]

[16] Lovecka, P.; Lipov, J.; Thumova, K.; Macurkova, A. *Curr. Pharm. Biotechnol.* **2017**, *18*, 1167. [Crossref]

[17] Lacatusu, I.; Badea, G.; Popescu, M.; Bordei, N.; Istrati, D.; Moldovan, L.; Seciu, A. M.; Panteli, M. I.; Rasit, I.; Badea, N. *Ind. Crops Prod.* **2017**, *109*, 141. [Crossref]

[18] Ahmad, N. M.; Mohamed, A. H.; Zainal-Abidin, N.; Nawahwi, M. Z.; Azzeme, A. M. *Inorg. Chem. Commun.* **2024**, *161*, 111839. [Crossref]

[19] Panneerselvam, C.; Alshehri, M. A.; Saif, A.; Faridi, U.; Khasim, S.; Mohammedsaleh, Z. M.; Parveen, H.; Omer, N.; Alasmari, A., Mukhtar, S.; Al-Aoh, H. A. *Polyhedron* **2024**, *257*, 117022. [Crossref]

[20] Zarate-Escobedo, J.; Zavaleta-Mancera, H. A.; Soto-Hernández, R. M.; Pérez-Rodríguez, P.; Vilchis-Nestor, A. R.; Silva-Rojas, H. V.; Trejo-Téllez, L. I. *Plants* **2024**, *13*, 981.[Crossref]

[21] Nandi, A.; Giram, H. S.; Patel, V. P.; Mehera, R.; Das, S.; Choudhary, D. K.; Das, N. *Naturforsch. A.* **2024,** *79*, 141. [Crossref]

[22] Burlec, A. F.; Hăncianu, M.; Macovei, I.; Mircea, C.; Fifere, A.; Turin-Moleavin, I. A.; Corciovă, A. *Appl. Sci.* **2022**, *12*, 887. [Crossref]

[23] Saini, V.; Thakur, A.; Verma, M.; Bharti, R.; Sharma, R. *Orbital: Electron. J. Chem.* **2024**, 293. [Crossref]

[24] Kaushik, P.; Bharti, R.; Sharma, R.; Verma, M.; Olsson, R. T.; Pandey, A. *Eur. Polym. J.* **2024**, 113574. [Crossref]

[25] Yadav, A.; Bharti, R. *Orbital: Electron. J. Chem.* **2024**, *16*, 205. [Crossref]

[26] Singh, A.; Bharti, R.; Thakur, A.; Verma, M.; Sharma, R. *Orbital: Electron. J. Chem.* **2024**, *16*, 271. [Crossref]

[27] Bansal, S.; Bharti, R.; Thakur, A.; Verma, M.; Sharma, R. *Orbital: Electron. J. Chem.* **2024**, *16*, 240. [Crossref]

[28] Thakur, A.; Verma, M.; Bharti, R.; Sharma, R. *Curr. Chin. Sci.* **2023**, *3*, 322. [Crossref]

[29] Chowdhury, A. S.; Islam, M. M.; Ghosh, A. (2024, June). In *Proceedings of the 14th International Conference on Mechanical Engineering (ICME 2023)*. [Crossref]

[30] Katta, V. K. M.; Dubey, R. S. *Materials Today: Proceedings* **2021**, *45*, 794. [Crossref]

[31] Erenler, R.; Geçer, E. N.; Genç, N.; Yanar, D. *Int. J. Chem. Technol*. **2021**, *5*, 141. [Crossref]

[32] Dhuldhaj, U. P.; Deshmukh, S. D.; Gade, A. K.; Yashpal, M.; Rai, M. K. *Nusantara Bioscience* **2012**, *4*, 109. [Crossref]

[33] Tyagi, P. K.; Tyagi, S.; Gola, D.; Arya, A.; Ayatollahi, S. A.; Alshehri, M. M.; Sharifi-Rad, J. *J. Nanomater*. **2021**, *1*, 6515419. [Crossref]

[34] Fiore, T.; Pellerito, C. *Charact.* **2021**,129. [Crossref]

[35] Saini, A.; Kumar, S.; Kaur, H.; Gaur, J.; Singh, G.; Kaur, M.; Kumar, S.; Limbu, R.; Supreet, P. N. Kaur, N. *Interactions* **2024**, *245*, 174. [Crossref]

[36] Sadiq, H.; Sher, F.; Sehar, S.; Lima, E. C.; Zhang, S.; Iqbal, H. M.; Zafar, F.; Nuhanović, M. *J. Mol. Liq.* **2021**, *335*, 116567. [Crossref]

[37] Farkas, N.; Kramar, J. A. *J. Nanopart. Res.* **2021**, *23*, 120. [Crossref]

[38] Muzafar, W.; Kanwal, T.; Rehman, K.; Perveen, S.; Jabri, T.; Qamar, F.; Faizi, S.; Shah, M. R. *J. Mol. Struct.* **2022**, *1269*, 133824. [Crossref]

[39] Rabani, G.; Dilshad, M.; Sohail, A.; Salman, A.; Ibrahim, S.; Zafar, I.; Arshad, H. M. *J. Chem.* **2023**, *1*, 4659034. [Crossref]

[40] Saxena, A.; Prasad, D.; Thakur, K. K.; Kaur, J. *AJSE* **2021**, *46*, 436. [Crossref]

[41] Agbaffa, E. B.; Akintemi, E. O.; Uduak, E. A.; Oyeneyin, O. E. *Sci. Lett.* **2021**, *15*, 42. [Crossref]

[42] Kayani, Z. N.; Arshad, S.; Riaz, S.; Naseem, S. *IEEE Trans. Magn.* **2014**, *50*, 1. [Crossref]

[43] Janjua, M. R. S. A.; Jamil, S.; Jahan, N.; Khan, S. R.; Mirza, S. *Chem. Cent. J.* **2017**, *11*, 1. [Crossref]

[44] Demirezen, D. A.; Yıldız, Y. Ş.; Yılmaz, Ş.; Yılmaz, D. D. JBB **2019**, *127*, 241. [Crossref]

[45] Rahman, M. M.; Jamal, A.; Khan, S. B.; Faisal, M. *J. Nanoparticle Res.* **2011**, *13*, 3789. [Crossref]

[46] Hwang, S. J.; Lee, J. H. *FS&T.* **2023,** *43*, 121522. [Crossref]

[47] Prakash, R.; Bharti, R.; Thakur, A.; Verma, M.; Sharma, R. *SCE* **2025**, *11*, 21. [Crossref]

[48] Rabani, G.; Dilshad, M.; Sohail, A.; Salman, A.; Ibrahim, S.; Zafar, I.; Arshad, H. M. *J. Chem.* **2023**, *1*, 4659034. [Crossref]

[49] Sandhya, J.; Kalaiselvam, S. *Mater. Res. Express.* **2020**, *7*, 015045. [Crossref]

[50] Erenler, R.; Gecer, E. N. *J. Nano R.* **2022**, *75*, 28. [Crossref]

[51] Raghavendra, N.; Mahesh, R. T.; Mahanthesh, B.; Mackolil, J. *Int. J. Biol. Macromol.* **2022,** *195*, 345. [Crossref]

[52] Kolawole, F. O.; Kolawole, S. K.; Owa, F. A.; Adebayo, A. O.; Ajibola, O. O.; Hassan, S. B. *SAM* **2023**, 453. [Crossref]

[53] Asaad, M. A.; Sarbini, N. N.; Sulaiman, A.; Ismail, M.; Huseien, G. F.; Majid, Z. A.; Raja, P. B. *J. Ind. Eng. Chem*. **2018**, *63*, 211. [Crossref]

[54] Anadebe, V. C.; Onukwuli, O. D.; Omotioma, M.; Okafor, N. A. *Mater. Chem. Phys*. **2019** *231*, 121033. [Crossref]

How to cite this article

Sharma, S.; Bharti, R.; Thakur, A.; Sharma, R.; Verma, M. *Orbital: Electron. J. Chem*. **2025**, *17*, 444. DOI: **http://dx.doi.org/10.17807/orbital.v17i5.22919**